Results in Engineering 24 (2024) 102875

Contents lists available at ScienceDirect

Results in Engineering

journal homepage: www.sciencedirect.com/journal/results-in-engineering

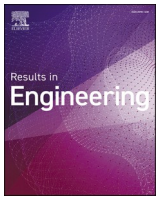

Superior photocatalytic degradation of pharmaceuticals and antimicrobial Features of iron-doped zinc oxide sub-microparticles synthesized via laser-assisted chemical bath technique

Samer H. Zyoud [a,b,c,*], Che Azurahanim Che Abdullah [d,e], Akram Ashames [b,f], Nageeb Hassan [b,f], Ibrahim S. Yahia [b,g,h,i], Ahed H. Zyoud [j], Heba Y. Zahran [g,h,i], Naser Qamhieh [k], Ghaseb N. Makhadmeh [l], Tariq AlZoubi [m]

[a] Department of Mathematics and Sciences, Ajman University, Ajman, P.O. Box 346, United Arab Emirates
[b] Center of Medical and Bio-Allied Health Sciences Research, Ajman University, Ajman, P.O. Box 346, United Arab Emirates
[c] School of Physics, Universiti Sains Malaysia (USM), Penang, 11800, Malaysia
[d] Nanomaterial Synthesis and Characterization Laboratory, Institute of Nanoscience and Nanotechnology, Universiti Putra Malaysia, Serdang, 43400, Selangor, Malaysia
[e] Biophysics Laboratory, Faculty of Science, Universiti Putra Malaysia, Serdang, 43400, Selangor, Malaysia
[f] Department of Clinical Sciences, College of Pharmacy and Health Sciences, Ajman University, P.O. Box 346, Ajman, United Arab Emirates
[g] Laboratory of Nano-Smart Materials for Science and Technology (LNSMST), Research Center for Advanced Materials Science (RCAMS), King Khalid University, Abha, 61413, P.O. Box 9004, Saudi Arabia
[h] Research Center for Advanced Materials Science (RCAMS), King Khalid University, Abha, 61413, P.O. Box 9004, Saudi Arabia
[i] Nanoscience Laboratory for Environmental and Biomedical Applications (NLEBA), Metallurgical Lab.1., Department of Physics, Faculty of Education, Ain Shams University, Roxy, Cairo, 11757, Egypt
[j] Department of Chemistry, SSERL, An-Najah National University, Nablus, Palestine
[k] Department of Physics, United Arab Emirates University, Al-Ain, United Arab Emirates
[l] General Education Department, Skyline University College, Sharjah, United Arab Emirates
[m] College of Engineering and Technology, American University of the Middle East, Egaila, 54200, Kuwait

ARTICLE INFO

Keywords:
Undoped and Fe-Doped ZnO
LACBS
Photocatalytic efficiency
Antimicrobial efficacy
Paracetamol
XRD
SEM
FTIR

ABSTRACT

Addressing the dual challenges of antimicrobial resistance and pharmaceutical contamination in wastewater is crucial for global health and environmental preservation. Predictions estimate up to 10 million annual deaths by 2050 due to antimicrobial resistance, underscoring the urgent need for innovative solutions. This study explores the potential of zinc oxide Sub-Microparticles (ZnO SMPs) doped with iron (Fe) to enhance the photocatalytic degradation of pharmaceutical compounds in water and improve antimicrobial efficacy. A green laser-assisted chemical bath synthesis method created ZnO SMPs with varying Fe dopant concentrations (1 %, 1.5 %, and 3 %). The synthesized Sub-Microparticles underwent rigorous structural analysis using X-ray diffractometry, SEM, EDX, FTIR, and UV–visible spectrophotometry techniques. Their photocatalytic performance was evaluated in the degradation of paracetamol under blue laser light, and their antimicrobial properties were assessed following CLSI guidelines. Structural analyses confirmed the hexagonal wurtzite structure of ZnO SMPs, with noticeable changes due to Fe doping, including a transition from sub-microrods to sub-microsheets and a redshift in the optical band gap. Photocatalytic tests revealed a significant enhancement in paracetamol degradation efficiency, increasing from 53.41 % with pure ZnO to 98.99 % with 3 % Fe-doped ZnO in 50 min. Antimicrobial assays demonstrated an increased inhibitory effect against pathogens, with Fe-doped ZnO outperforming control discs. This study substantiates the potential of Fe-doped ZnO SMPs in wastewater treatment and antimicrobial applications, showcasing significant improvements in photocatalytic degradation of pharmaceutical compounds and antimicrobial efficacy. The findings underscore the importance of continuing research in this domain for environmental and public health benefits.

* Corresponding author.
E-mail address: s.zyoud@ajman.ac.ae (S.H. Zyoud).

https://doi.org/10.1016/j.rineng.2024.102875
Received 22 June 2024; Received in revised form 21 August 2024; Accepted 8 September 2024
Available online 10 September 2024

1. Introduction

In recent years, the environmental impact of pharmaceuticals has emerged as a critical concern, highlighting the urgent need for effective remediation strategies [1,2]. Pharmaceuticals, characterized by their persistence and bioaccumulation, are increasingly detected in aquatic ecosystems due to inadequate removal during conventional wastewater treatment processes [3,4]. Consequently, these contaminants enter natural water bodies, causing ecological and health issues and contributing to antimicrobial resistance [1,5].

The challenge in degrading pharmaceuticals lies in their complex molecular structures and chemical properties, making conventional methods insufficient [2,4]. Advanced oxidation processes, like photocatalysis, offer a potential solution by using highly reactive species to break down complex pollutants into less harmful substances [6,7]. Zinc oxide (ZnO), a semiconductor with a wide band gap of about 3.37 eV and a large exciton binding energy of 60 meV, shows exceptional photocatalytic activity under UV light due to its ability to generate electron-hole pairs [8–10].

However, ZnO's photocatalytic efficiency is limited by its wide band gap, restricting its absorption to the UV region, a small fraction of the solar spectrum [11]. Efforts are underway to modify ZnO to absorb visible light, enhancing its practical applicability for degrading a broader range of pollutants [12,13]. The rapid recombination of photo-generated electron-hole pairs in ZnO also hampers its photocatalytic performance [14]. Doping ZnO with transition metals, such as iron, introduces new energy levels that reduce recombination rates, improving overall photocatalytic activity [15,16].

Iron doping narrows ZnO's band gap, allowing it to absorb more visible light, thus enhancing photocatalytic activity [6,17]. It also reduces electron-hole pair recombination by creating trap sites, extending their lifespan, and increasing the likelihood of pollutant degradation [11,12]. Iron's multiple oxidation states (Fe^{2+} and Fe^{3+}) facilitate various redox reactions, further boosting the degradation of complex organic pollutants, including pharmaceuticals [18]. Iron-doped ZnO nanoparticles also exhibit enhanced antimicrobial properties. The interaction between iron ions and microbial cells generates reactive oxygen species (ROS), which are lethal to many microorganisms [19,20]. This dual functionality—efficient pollutant degradation and antimicrobial activity—makes Fe-doped ZnO nanoparticles valuable for environmental remediation and public health protection [20,21].

The laser-assisted chemical bath synthesis (LACBS) technique for synthesizing Fe-ZnO nanoparticles ensures controlled and uniform iron incorporation into the zinc oxide matrix [8,22,23]. This method allows precise tuning of iron doping concentration, which is critical for optimizing photocatalytic and antimicrobial properties. Excessive doping can lead to visible light shielding, decreased surface area, and larger particles, diminishing photocatalytic activity [24,25]. The laser-assisted technique also promotes well-defined nanoparticle sizes and shapes, which is crucial for maximizing surface area and active sites for photocatalytic reactions [8,26]. The thermal effects of the laser enhance the crystalline structure, ensuring robustness and stability under operational conditions, which are essential for long-term environmental applications [27,28]. This study assesses the performance of iron-doped sub-microparticles (ZnO SMPs), synthesized via LACBS, against diverse pathogens and their capability to degrade pharmaceuticals. The goal is to comprehensively understand the nanoparticles' antimicrobial efficacy, mechanisms of action, and contributions to environmental sustainability.

2. Materials and methods

2.1. Experiment Setup

The experiment utilized materials and supplies, including Hexamethylenetetramine (HMTA), Zinc acetate dihydrate, deionized water, Iron (III) chloride, and paracetamol. For microbial assays, the organisms employed were *Escherichia coli*, *Staphylococcus aureus*, *Candida albicans*, *Klebsiella pneumonia*, and *Bacillus subtilis*. The culture media used included Sabouraud Dextrose broth and Mueller-Hinton Broth. Additional supplies for the assays included sterilized filter paper discs, single-use Petri dishes, McFarland standard sets, and antibiotics such as gentamicin and nystatin.

2.2. Catalyst preparation

Three solutions were prepared: solution A with 2.195g of zinc acetate in 50 mL deionized water, solution B with 1.402g of HMTA in 50 mL deionized water, and solution C with 1.622g of iron chloride in 50 ml deionized water. All solutions were adjusted to 0.2 M and underwent stirring and sonication for complete solute dissolution.

2.3. Synthesis method

Undoped ZnO sub-micro-powders were synthesized by mixing solution B into solution A, with constant stirring at ambient temperature for 15 min, followed by green laser irradiation (532 nm wavelength, 10 W power). This mixture was stirred magnetically at 65 °C for 90 min to form ZnO ZnO SMPs. Post-formation, these structures were filtered, thoroughly washed with ethanol, dried at 110 °C for 25 min, and

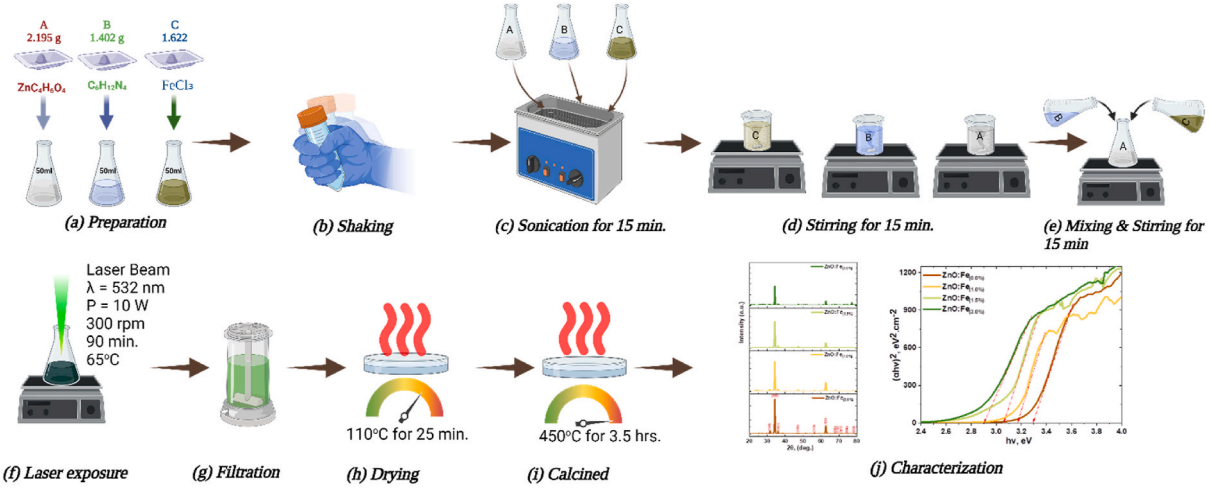

Fig. 1. Schematic of synthesis process for pure and Fe-doped ZnO SMPs.

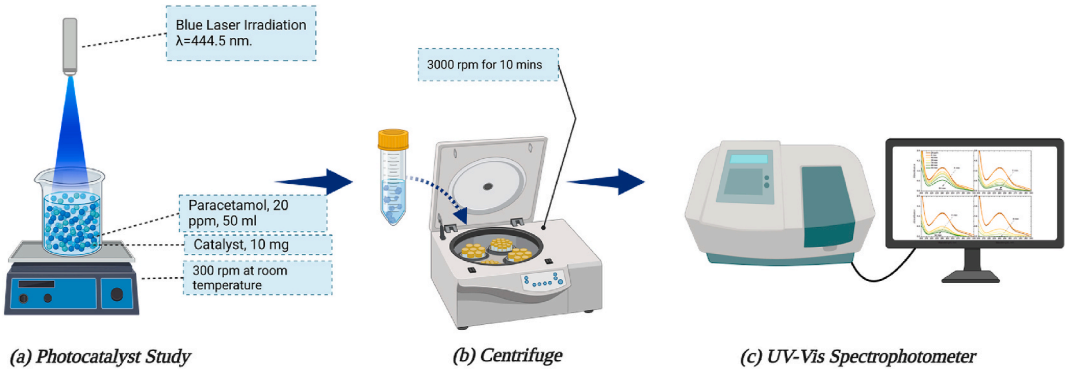

Fig. 2. Diagram of working principles.

annealed at 450 °C for 3.5 h for purification and impurity removal.

We employed a similar procedure to produce Fe-doped ZnO sub-micro-powders using solutions A, B, and C. For a comprehensive understanding of the steps involved in synthesizing both undoped and Fe-doped ZnO ZnO SMPs, one can refer to the illustrative details provided in Fig. 1.

2.4. Determination of zinc oxide properties

Advanced analytical techniques were used to analyze the crystal characteristics of the specimens. Phase and structural analysis were conducted using a Rigaku X-ray diffractometer (XRD). A JEOL JSM-7600F Scanning Electron Microscope (SEM) and Energy-Dispersive X-ray (EDX) analysis examined the surface topography and chemical composition of ZnO SMPs. Fourier-Transform Infrared Spectroscopy (FTIR) assessed the molecular structure of iron-doped ZnO, while an Ultraviolet–Visible (UV–Vis) spectrophotometer (PE lambda 750S model) and a UV–Vis spectrum analyzer determined and confirmed the optical absorption properties.

2.5. Photocatalytic activity experiments

Photocatalytic tests were conducted at room temperature using a 444.5 nm blue laser light. The procedure involved mixing 10 mg of catalysts with 20 ppm paracetamol solution, stirring it, and allowing it to sit in darkness for 20 min to achieve adsorption-desorption equilibrium. Upon irradiation, 5 mL samples were extracted every 10 min for analysis. UV–visible spectroscopy was used to analyze these samples, detecting peak paracetamol absorption at 240.58 nm (see Fig. 2). The degradation rate and efficiency were quantified using established equations (1) and (2) [29].

$$ln\frac{C_o}{C} = k_{app}t, \tag{1}$$

$$PDE\% = \left(1 - \frac{C}{C_o}\right) \times 100\ \%, \tag{2}$$

Samples were extracted every 10 min for 50 min, filtered, and analyzed via UV–visible spectroscopy to monitor the degradation of paracetamol at its absorption peak of 240.58 nm. Control experiments without catalysts were also performed to account for natural photolysis of the compound. Data analysis involved plotting ln(C₀/C) against time to determine the rate constants using a first-order kinetic model, and photodegradation efficiencies were calculated to quantify the catalyst performance.

2.6. Structural parameters and optical bandgap calculations

Using the LACBS technique, undoped and doped ZnO SMPs were synthesized and analyzed for structural properties. Key focus areas included the 002 diffraction peak characteristics like peak position (2θ), intensity, full width at half maximum FWHM, lattice constants (a, b, c), and internal strain stress (ε_a, ε_c). XRD was the primary method used, applying Bragg's equation (Eq. (3)) to estimate residual stress in the ZnO SMPs [30,31].

The Debye-Scherer formula (Eq. (4)) was used to analyze the crystal structure and size of ZnO samples, considering a constant ($k = 0.94$), the Bragg angle (θ), X-ray wavelength (λ = 1.5427), and FWHM (β). The study focused on HMTA exposure duration. Lattice constants (a, b, c) for both doped and undoped ZnO were calculated using Eqs. (5) and (6). Baseline constants (a_o, c_o) were obtained from X-ray diffraction. Perpendicular strain (ε_a) and c-axis strain (ε_c) in ZnO films were quantified using Eq. (7) and Eq. (8), respectively, with films developed on Kapton tape substrates [30,32].

$$n\lambda = 2dsin\theta, \tag{3}$$

$$D(\text{Å}) = \frac{k\lambda}{\beta\ cos\ \theta}, \tag{4}$$

$$a(\text{Å}) = b(\text{Å}) = \frac{\lambda}{\sqrt{3}sin\ \theta} \tag{5}$$

$$c(\text{Å}) = \frac{\lambda}{sin\ \theta} \tag{6}$$

$$\varepsilon_a = \frac{a - a_o}{a_o} \times 100\ \%, \tag{7}$$

$$\varepsilon_c = \frac{c - c_o}{c_o} \times 100\ \%, \tag{8}$$

The optical bandgaps were calculated using Eqs. (9) and (10), incorporating constants like the absorption coefficient (α), light speed (c), Planck's constant (h), absorption constant (A), maximum absorption wavelength (λ), and a semiconductor-specific constant ($n = 2$ for direct bandgap, ½ for indirect) Eq. (10) was used for analyzing the optical properties, and Fig. 6 shows the ZnO sub-microsheets' optical energy bandgap data [29].

$$E_g(eV) = \frac{hc}{\lambda(nm)} = \frac{1240}{\lambda(nm)}, \tag{9}$$

$$(\alpha h\nu)^n = A\left(h\nu - E_g\right), \tag{10}$$

2.7. Microbial assay

The antimicrobial efficacy of iron-doped zinc oxide was assessed following the Clinical and Laboratory Standards Institute guidelines [33]. Bacterial strains were grown in Mueller Hinton Broth at 37 °C and C. albicans in Sabouraud Dextrose broth at 30 °C for at least 4 h. Then, 100 μL of these cultures were placed onto sterile Mueller Hinton Agar

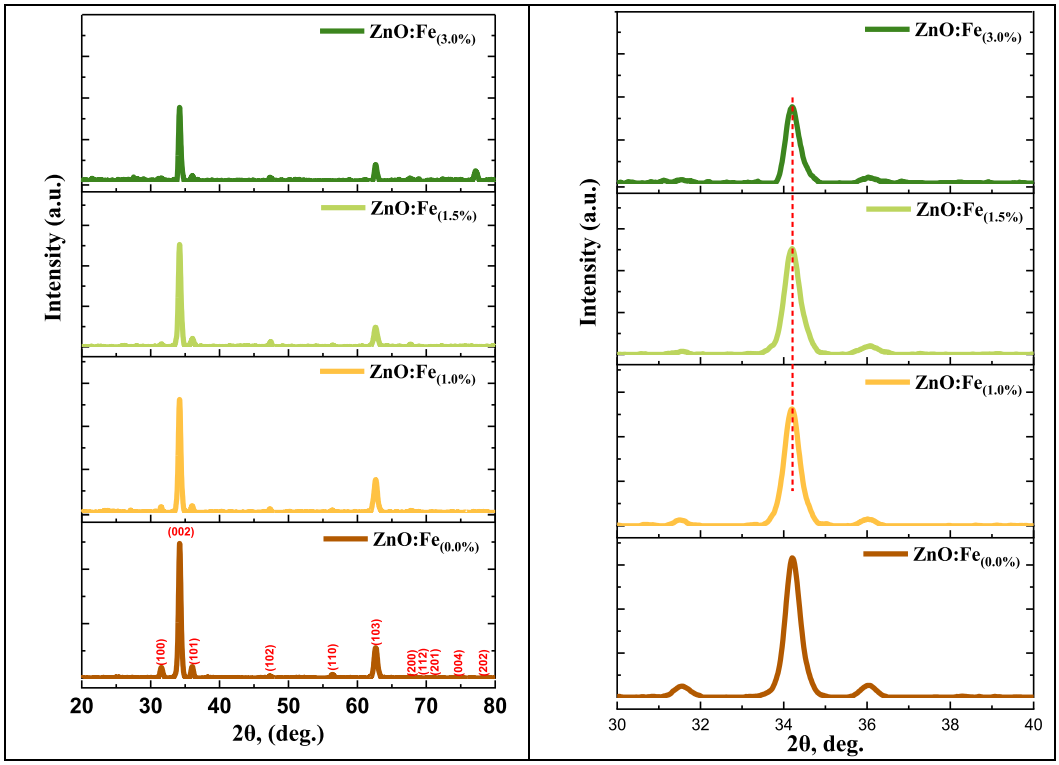

Fig. 3. XRD of pure & Fe-doped ZnO SMPs.

Table 1
Lattice parameters and structure of pure and FE-doped ZnO [(002) diffraction peak].

Samples	2 θ, (deg)	d	β, (Rad.)	I	D, (nm)	a = b, (nm)	c, (nm)	ε_a	ε_c
Pure ZnO	34.21	2.6264	0.00752	580	19.2867	0.3025	0.5240	−6.8847	0.7080
ZnO:Fe$_{(1\ \%)}$	34.21	2.6243	0.00753	348	19.2599	0.3025	0.5240	−6.8847	0.7080
ZnO:Fe$_{(1.5\ \%)}$	34.20	2.6381	0.00754	284	19.2550	0.3026	0.5242	−6.8583	0.7366
ZnO:Fe$_{(3\ \%)}$	34.18	2.6242	0.00754	159	19.2450	0.3028	0.5245	−6.8054	0.7938

plates. Control discs were soaked in nystatin and gentamicin, whereas test filter paper discs received 1 mL of sub-microcolloid and were dried for 24 h. The inhibition zones were measured to the nearest millimeter. A Zone of Inhibition (ZOI) of zero indicated resistance; any visible zone suggested susceptibility.

3. Results

3.1. X-ray diffraction results

Fig. 3 displays the XRD patterns of four samples. The undoped ZnO shows hexagonal wurtzite structure peaks, indicating single-phase crystallinity with c-axis orientation. Fe-doped ZnO samples have sharper, less intense peaks, with no iron oxide peaks, maintaining hexagonal wurtzite crystal clarity. ZnO:Fe samples (1 %, 1.5 %, 3 %) exhibit pronounced (002) lattice plane peaks. Increased doping levels result in leftward diffraction angle shifts, reduced peak intensity, and wider FWHM.

Table 1 illustrates the computed strain values, where negative numbers signify the occurrence of compressive stress. A correlation was noted between the shift in the diffraction angle of the (002) peak and a diminished d-spacing, following Bragg's Law. Alterations in the growth conditions, notably the duration of HMTA exposure, were pivotal in influencing the crystal morphology. This variable was instrumental in steering grain growth and led to the decomposition of HMTA into OH^- ions, thereby promoting the combination of Zn^+ and OH^- ions and consequently increasing the size of the ZnO crystals. The lattice constants (a, b, and c) for the ZnO specimens aligned with the established standards in the Joint Committee on Powder Diffraction Standards (JCPDS) card no. 01-079-0206, with the standard lattice constants for ZnO thin films documented as a_o = 3.2494 Å and c_o = 5.2038 Å. Additionally, the bond lengths of ZnO measured in this research were consistent with the acknowledged literature value of 1.9767 Å.

Table 1 also encapsulates the structural parameters of the ZnO SMPs synthesized through the LACBS method. The majority of these parameters remained stable across varying doping concentrations. Nonetheless, an evident decrease in diffraction intensity was observed when the doping levels were increased. The detected strains in these materials were deduced to stem from intrinsic and extrinsic origins, with extrinsic strains being attributed to defects and impurities.

3.2. Scanning Electron Microscope

This study used SEM to examine the morphology of pristine ZnO and Iron-doped ZnO (1 %, 1.5 %, 3 %) ZnO SMPs. SEM images (Fig. 4) revealed a morphological change from hexagonal sub-microrods in undoped ZnO to densely packed ZnO sub-microsheets with Iron doping. The sub-microsheets grew non-perpendicularly to the substrate and exhibited a dominant (002) peak. While ZnO sub-microrods had a wurtzite lattice, the sub-microsheets showed an increased aspect ratio.

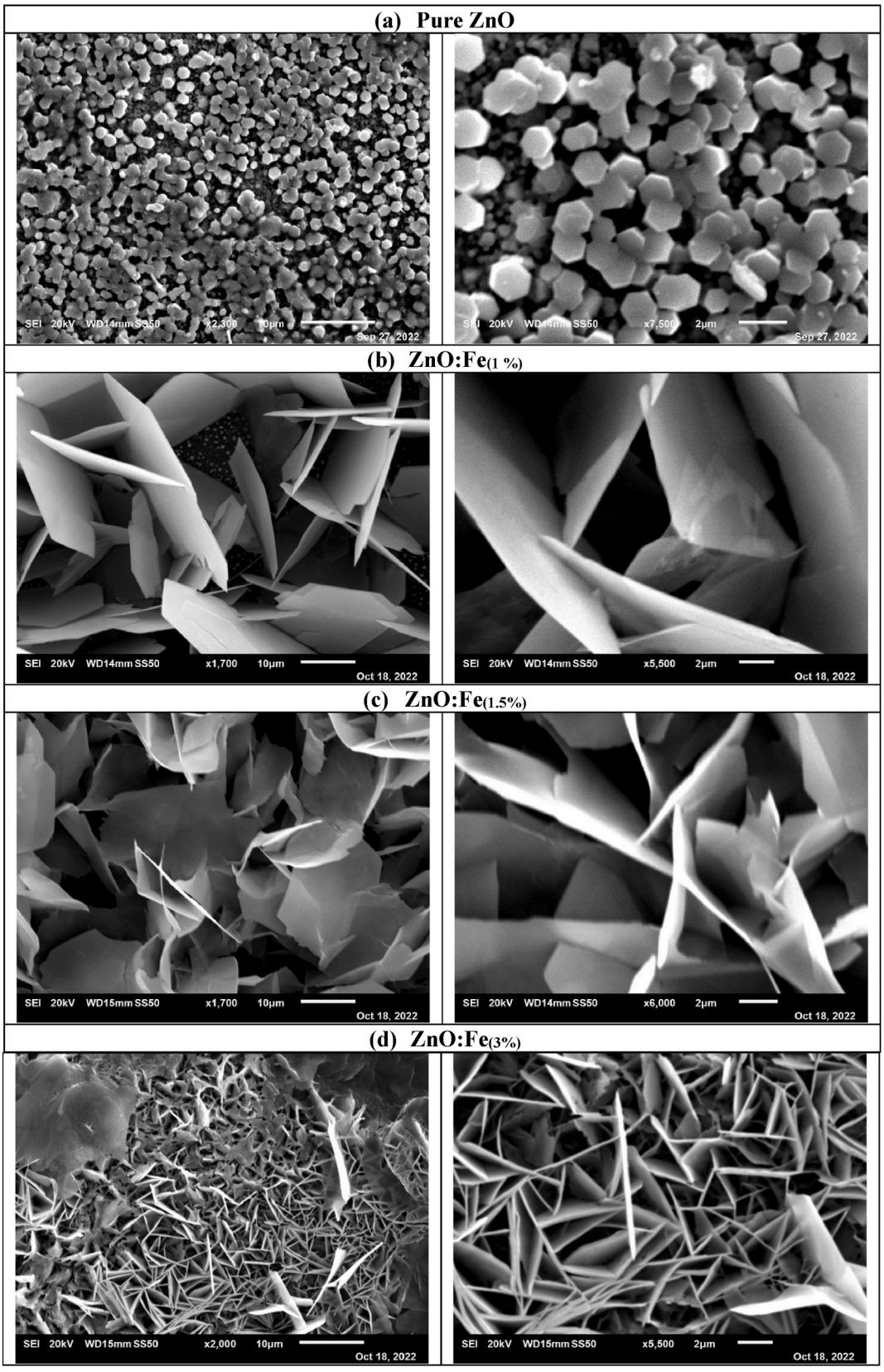

Fig. 4. SEM images: (a) ZnO, (b) ZnO:$Fe_{(1\ \%)}$, (c) ZnO:$Fe_{(1.5\ \%)}$, (d) ZnO:$Fe_{(3\ \%)}$, synthesized via LACBS.

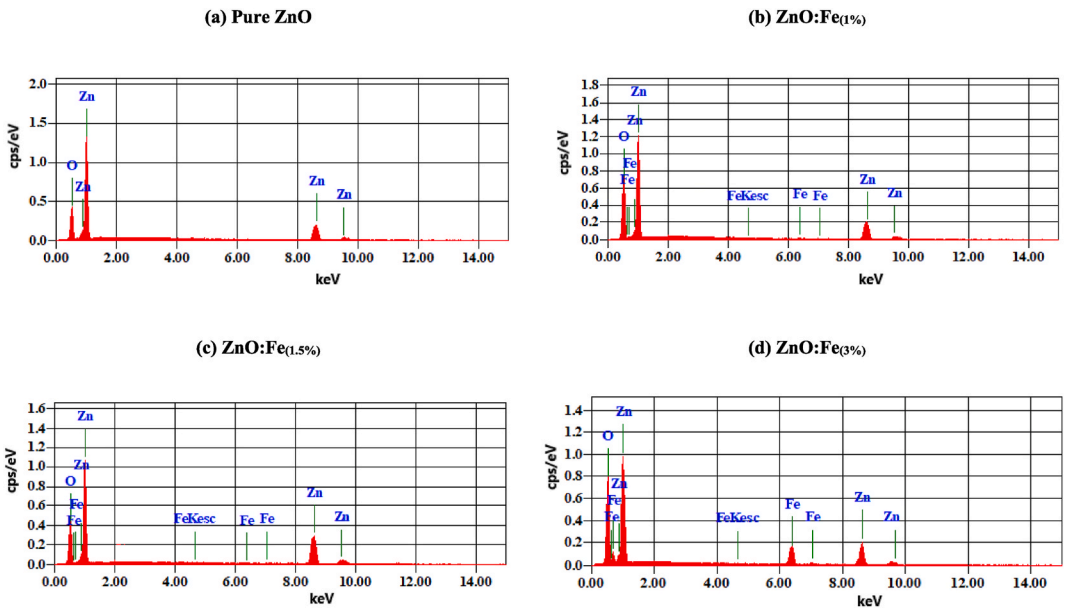

Fig. 5. EDX spectra of (a) Pure ZnO, (b) ZnO:$Fe_{(1\ \%)}$, (c) ZnO:$Fe_{(1.5\ \%)}$, (d) ZnO:$Fe_{(3\ \%)}$.

3.3. Energy dispersive X-ray spectroscopy

To investigate the elemental makeup of the produced sub-micropowders, EDX spectroscopy was employed, focusing on undoped ZnO and ZnO integrated with various Fe concentrations (1 %, 1.5 %, and 3 %). The outcomes, displayed in Fig. 5, authenticated the existence of Zn, O, and Fe within all the samples subjected to the analysis. Notably, the sample of pure ZnO revealed a stoichiometric balance between zinc and oxygen, with their proportions being 47.66 % for Zn and 52.34 % for O, respectively. Furthermore, an elaborate elemental analysis of the samples enriched with Fe is meticulously cataloged in Table 2.

3.4. UV–Vis absorption

The UV–visible absorption spectra (Fig. 6) showed that undoped ZnO had an absorption edge at 376.89 nm (3.29 eV band gap) with a significant shift indicating electron transitions. Fe doping caused a redshift in the absorption edge, lowering the band gap: 1 %, 1.5 %, and 3 % Fe-doped samples had direct band gaps of 3.17 eV, 3.06 eV, and 2.91 eV, respectively, and indirect band gaps of 2.85 eV, 2.66 eV, and 2.28 eV, compared to the undoped sample's 2.93 eV. These changes are graphically depicted in Fig. 6.

3.5. Fourier-transform infrared spectra

The FTIR analysis showed peaks from 500 to 600 cm^{-1}, indicating bond stretching modes, with Zn-O stretching vibrations in hexagonal zinc oxide crystals observed between 537 and 680 cm^{-1}. The characteristic ZnO band at approximately 530 cm^{-1} was noted in both undoped and Fe-doped ZnO SMPs (Fig. 7). Infrared spectroscopy of ZnO-based sub-microsheets revealed O-H stretching (3300-3700 cm^{-1}) due to hydroxyl groups or surface-adsorbed water, a 1500 cm^{-1} peak for $Zn(OH)_2$ bending vibrations, and symmetric/asymmetric C=O stretching vibrations. Peaks around 2350 cm^{-1} may be linked to CO_2 absorption from air and moisture on metal cation surfaces.

To enhance reproducibility in research involving the characterization of ZnO nanostructures, clear, detailed protocols for each analytical technique are essential. For XRD, ensure samples are finely ground, evenly distributed on the sample holder, and scanned from 20° to 80° 2θ using a Rigaku diffractometer. SEM imaging, using a JEOL JSM-7600F, requires samples to be mounted and possibly coated with a conductive material, followed by imaging at various magnifications to assess morphology. EDX should be integrated with SEM to provide elemental composition analysis under the same sample conditions. FTIR involves mixing the sample with potassium bromide to form pellets for transmission mode analysis on a Nicolet iS10 spectrometer. UV–Visible Spectroscopy measurements should be done on a PE Lambda 750S spectrophotometer, analyzing the absorption from 200 nm to 800 nm to determine the optical bandgap using the Tauc plot method. For photocatalytic activity experiments, disperse the catalyst in a paracetamol solution, allow equilibrium in darkness, then expose to a blue laser, sampling every 10 min for UV–Vis analysis of degradation rates. These protocols ensure systematic execution of characterization techniques, fostering reproducibility and reliability in results.

3.6. Photocatalyst study

3.6.1. Blue laser/UV–Vis photocatalytic degradation studies

The primary aim of this investigation was to explore the photocatalytic abilities of ZnO specimens, both in their pure form and when doped with Fe, in breaking down paracetamol. To carry out this analysis, the absorption spectra were scrutinized prior to and following irradiation with a blue laser (having a wavelength of 444.5 nm and light intensity of 7 W/cm^2), illustrated in Fig. 8. Every tested ZnO sample showcased a pronounced photocatalytic activity when subjected to the blue laser, evidenced by a steady reduction in the paracetamol absorption spectra as the duration increased. Notably, the ZnO sample that was augmented with Fe displayed a more potent photocatalytic performance due to its reduced band gap energy. Detailed insights into the photocatalytic degradation kinetics, crucial for calculating the rate of paracetamol breakdown, are provided in Table 3, where the natural logarithm $ln\left(\frac{C_o}{C}\right)$ of the initial concentration to the concentration at varying intervals is plotted against time.

The evaluation of photodegradation efficiency (*PDE*%) was carried out by applying Equation (2), which is visually represented in Fig. 9. This figure highlights a direct and proportional relationship between the extent of photocatalytic degradation and the duration of exposure to irradiation. In an experiment involving agitation under blue laser irradiation for 10 min, the adsorption percentages observed were 17.26 % for pure ZnO, 47.14 % for ZnO:$Fe_{(1\ \%)}$, 56.70 % for ZnO:$Fe_{(1.5\ \%)}$, and 66.94 % for ZnO:$Fe_{(3\ \%)}$. These values significantly increased after an

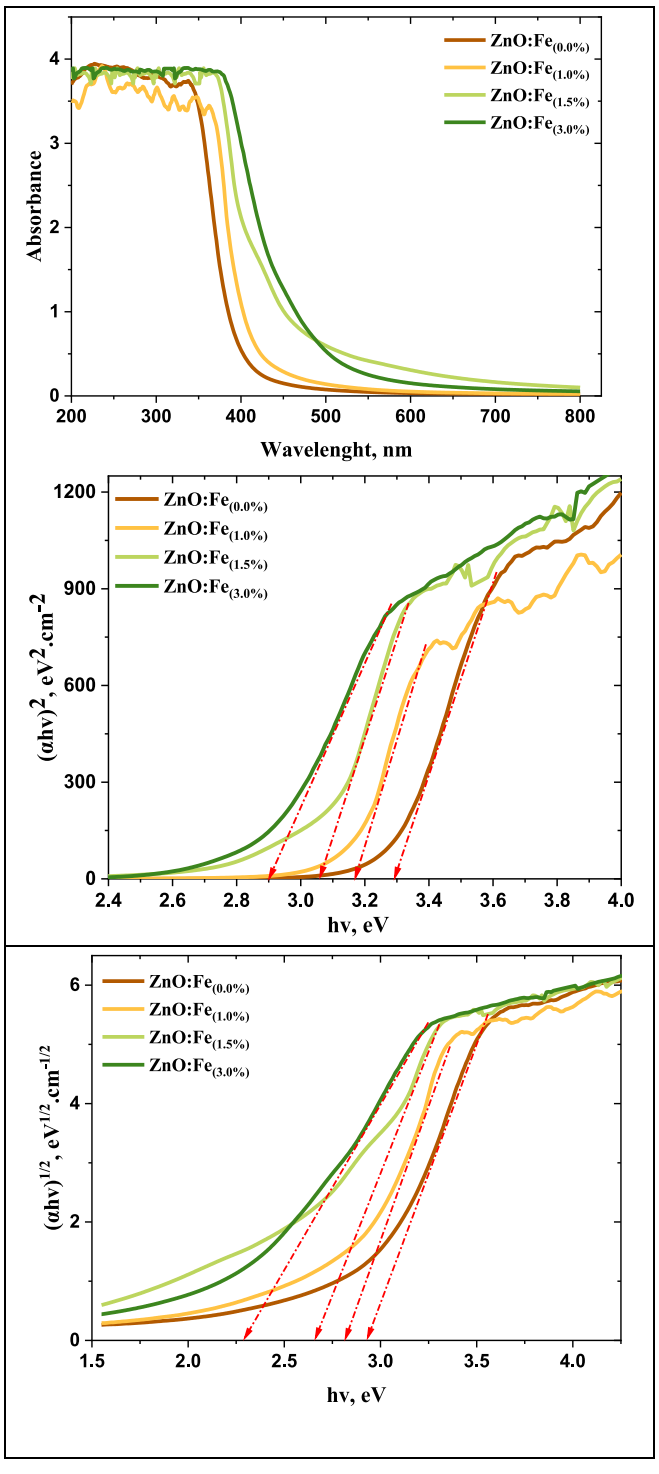

Fig. 6. (a) Absorbance spectra, (b) Direct band gap, and (c) Indirect band gap.

extended irradiation period of 50 min, reaching 53.41 %, 76.67 %, 78.89 %, and 98.99 % for the respective materials. The rate at which the pollutant degraded over time was also meticulously analyzed, employing photodegradation kinetics (C_o/C), with the findings presented in Fig. 10.

Fig. 11 displays the degradation of paracetamol using blue laser and zinc oxide photocatalysts, both undoped and iron-doped. The rate constants, calculated using Eq. (1), are in Table 3, comparing the efficiencies of undoped and Fe-doped ZnO. 3 % iron-doped ZnO has the highest efficiency.

Results indicated a superior photocatalytic activity of Fe-doped ZnO nanoparticles, with significant enhancements in degradation rates and efficiency compared to the undoped samples. These findings highlight the effectiveness of iron doping in enhancing the photocatalytic properties of ZnO, providing insights into the potential for optimized catalyst design in environmental applications.

3.6.2. *Photocatalytic stability*

The [ZnO:$Fe_{(3\ \%)}$] catalyst sample demonstrated consistent photostability when illuminated with a blue laser in freshly prepared paracetamol solutions. A slight decrease in photocatalytic degradation was observed across four subsequent experimental rounds following the initial test. The *PDE*% values were calculated using Equation (2). After stirring for 50 min under blue laser exposure in each cycle, the adsorption percentages were recorded as 97.86 % for the first cycle, 96.65 % for the second cycle, 96.01 % for the third cycle, and 94.83 % for the fourth cycle. Fig. 12 displays the paracetamol photodegradation rates through this series of experiments with the [ZnO:$Fe_{(3\ \%)}$] photocatalyst under blue laser illumination. Moreover, the XRD pattern of the [ZnO:$Fe_{(3\ \%)}$] catalyst sample, as depicted in Fig. 13, showed no evidence of degradation or phase instability after undergoing these four cycles.

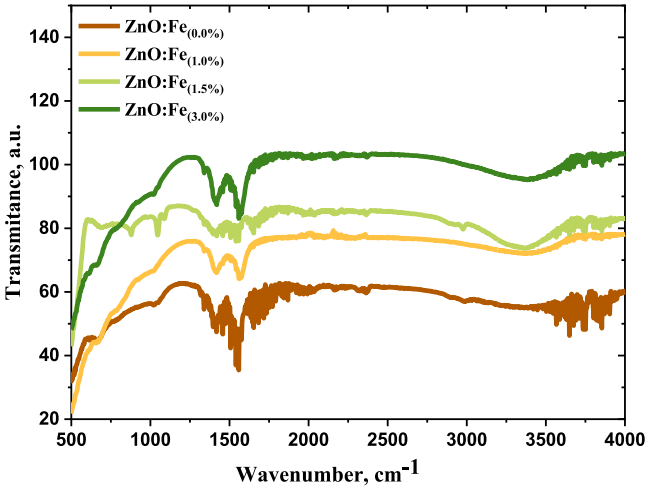

Fig. 7. FTIR spectra of pure and iron-doped ZnO SMPs.

Table 2
EDX of Fe-doped ZnO SMPs.

Samples	Pure ZnO		ZnO:$Fe_{(1\ \%)}$		ZnO:$Fe_{(1.5\ \%)}$		ZnO:$Fe_{(3\ \%)}$	
Elements	wt%	At%	wt%	At%	wt%	At%	wt%	At%
Zn	21.18	52.34	21.14	52.20	21.69	52.98	20.82	51.58
O	78.82	47.66	77.48	46.82	76.22	45.56	74.99	45.45
Fe	0	0	1.39	0.98	2.09	1.46	4.18	2.97
Total	100	100	100	100	100	100	100	100

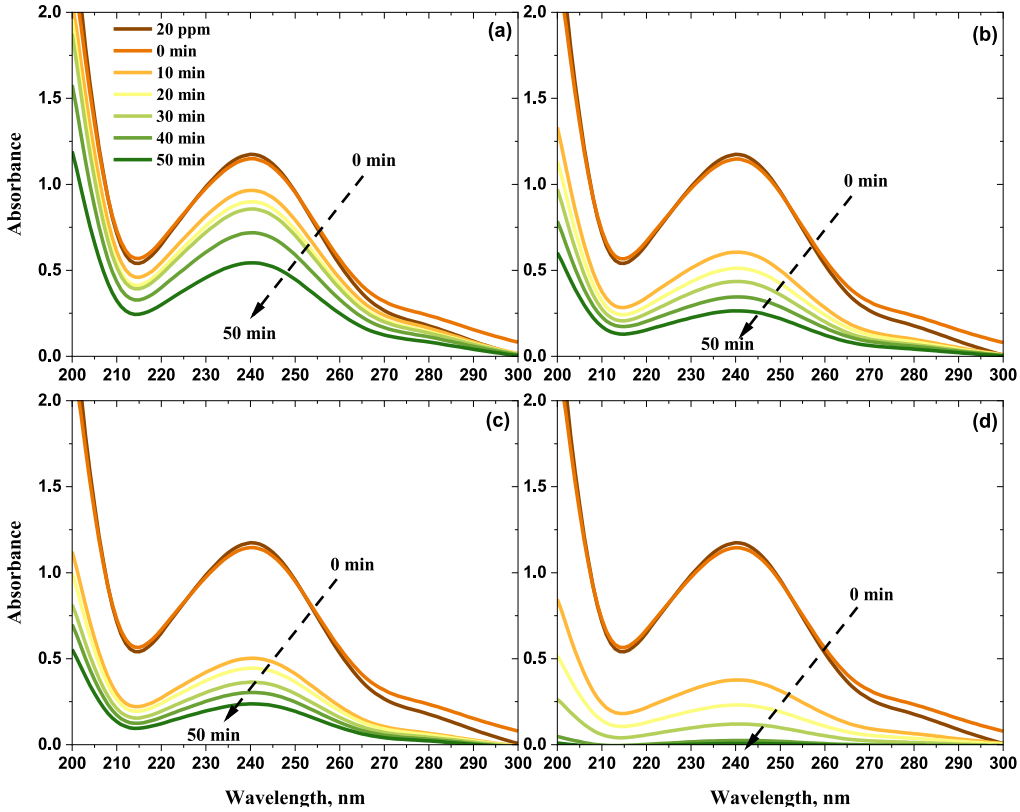

Fig. 8. UV–visible absorption of paracetamol with (a) ZnO, (b) 1 % ZnO:Fe, (c) 1.5 % ZnO:Fe, and (d) 3 % ZnO:Fe.

Table 3
Comparing efficiencies of catalysts with prior research.

Synthesis Method	Catalyst Type	Catalyst Amount	Pharmaceuticals	Light Source	% of Deg	k_{app}, (min^{-1})	Time, (min)	Refs.
Facile precipitation method	$ZnO:La_{(1.5\ \%)}$	1.0 wt%	Paracetamol (100 mg/L)	Visible light	99	–	180	[34]
Commercial	Pure ZnO 0.5 g/L	0.5 g/L	Ampicillin (105 mg/L)	UV	100	0.00056	300	[35]
Hydrothermal method	$ZnO:Ce_{(5\ \%)}$	5 mg/L	Paracetamol	Visible light	65	0.0022	250	[36]
Commercial	Pure ZnO 1.5 g/L	1.5 g/L	Metronidazole (80 mg/L)	UV	96.5	–	180	[37]
LACBS	**$ZnO:Fe_{(0\ \%)}$**	**10 mg/50 mL**	**Paracetamol (20 ppm)**	**Blue laser**	**53.41**	**0.0135**	**50**	**This work**
LACBS	**$ZnO:Fe_{(1\ \%)}$**	**10 mg/50 mL**	**Paracetamol (20 ppm)**	**Blue laser**	**76.67**	**0.0312**	**50**	**This work**
LACBS	**$ZnO:Fe_{(1.5\ \%)}$**	**10 mg/50 mL**	**Paracetamol (20 ppm)**	**Blue laser**	**78.89**	**0.0346**	**50**	**This work**
LACBS	**$ZnO:Fe_{(3\ \%)}$**	**10 mg/50 mL**	**Paracetamol (20 ppm)**	**Blue laser**	**98.99**	**0.0881**	**50**	**This work**

3.7. Antimicrobial activity of ZnO-NSs

3.7.1. Microorganism's ZOI

The study explored the antimicrobial properties of zinc oxide produced using LACBS, focusing its attention on several bacteria and fungi, namely Staphylococcus aureus, Bacillus subtilis, Escherichia coli, Klebsiella pneumonia, and Candida albicans. A detailed comparative analysis is provided in a table.

For S. aureus treated with a specific antibiotic, the data revealed that the inhibitory response was enhanced from using the antibiotic alone (28 ± 0.24) to the incorporation of pure ZnO (33 ± 0.18), with a further increase observed with different ZnO:Fe concentrations (35 ± 0.42, 35 ± 0.51, 40 ± 0.30). A contrasting pattern was noted for *Bacillus subtilis*, where the inhibitory effect reduced with the introduction of pure ZnO (15 ± 0.36) compared to the antibiotic alone (21 ± 0.28) but showed a positive shift with varying ZnO:Fe concentrations (18 ± 0.41, 20 ± 0.34, 23 ± 0.30).

In the case of *E. coli*, a steady uptrend in inhibitory effect was noted, ranging from the antibiotic alone (23 ± 0.33) to the highest concentration of ZnO:Fe (30 ± 0.31). For *K. pneumonia*, an upward trend in the inhibitory response was observed starting from the antibiotic alone (30 ± 0.10), escalating with the addition of pure ZnO (36 ± 0.23), and continuing to increase with various concentrations of ZnO:Fe (40 ± 0.37, 40 ± 0.33, 46 ± 0.18). Finally, with *C. albicans*, the absence of the specified antibiotic resulted in an inhibitory effect of (16 ± 0.42), which saw an increase with the addition of pure ZnO (30 ± 0.21) and remained relatively constant with increasing concentrations of ZnO:Fe (30 ± 0.42, 31 ± 0.32, 35 ± 0.43). These findings are presented in Table 4 and Fig. 15.

3.7.2. Comparing our results with previous studies

This article underscores the bactericidal capabilities of zinc oxide, corroborating its effectiveness against a spectrum of pathogens as previously established by numerous studies. Additionally, it draws attention to the heightened ZOI exhibited by zinc oxide when synthesized through the LACBS methodology compared to other methods against the pathogens examined. These insights necessitate further exploration into the distinctive attributes of LACBS-derived zinc oxide, particularly its potential integration into medical practices. To facilitate a holistic understanding of the ZOI variations across different research settings, a

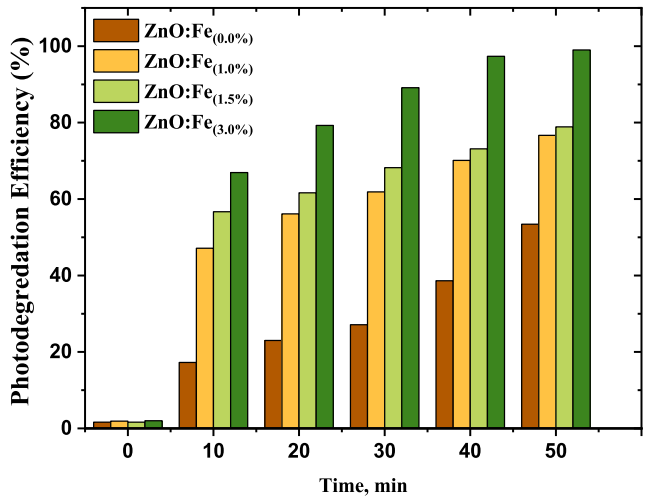

Fig. 9. Paracetamol degradation at various times with the different photocatalysts.

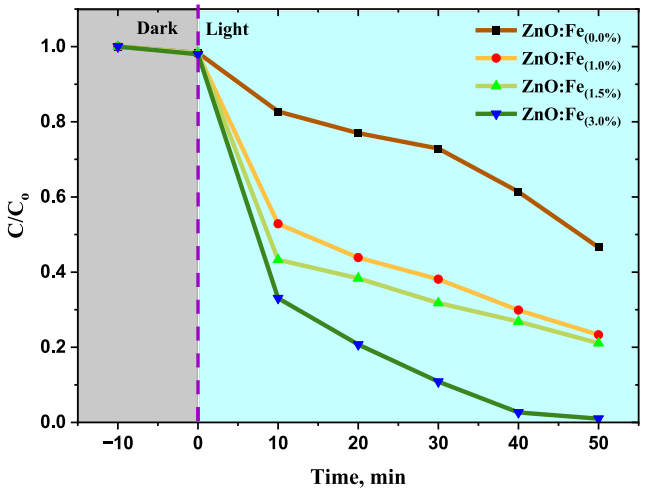

Fig. 10. Paracetamol concentration spectra.

comprehensive analysis is provided in Table 5, detailing the comparative results from various studies.

4. Discussion

Exploring ZnO's photocatalytic capabilities, particularly when enhanced through doping, has garnered considerable attention in materials science and environmental studies. This research delves into the effects of LACBS utilization on ZnO characteristics, alongside the impacts of varying iron doping levels on its antimicrobial and photocatalytic functionalities.

A prominent aspect of this research is the remarkable improvement in photocatalytic efficiency observed in samples of ZnO doped with iron. This finding is consistent with previous studies highlighting doping as a crucial mechanism for augmenting photocatalytic activity [17]. A deeper analysis reveals that the diminished band gap energy resulting from Fe-doping plays a significant role in this enhancement. A smaller band gap energy increases the probability of electron excitation from the valence band to the conduction band upon exposure to light [42]. This heightened electron movement produces reactive oxygen species, such as hydroxyl radicals, essential for breaking down pollutants [43]. Furthermore, the literature supports that oxygen vacancies are active

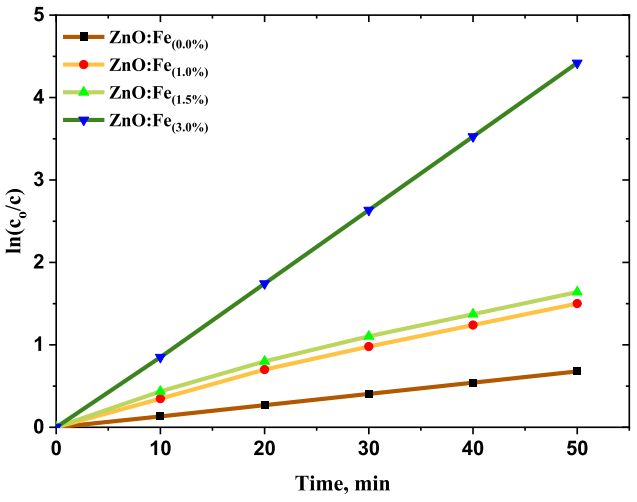

Fig. 11. A plot showing $ln\left(\frac{C_0}{C}\right)$ over time to calculate paracetamol rate constants.

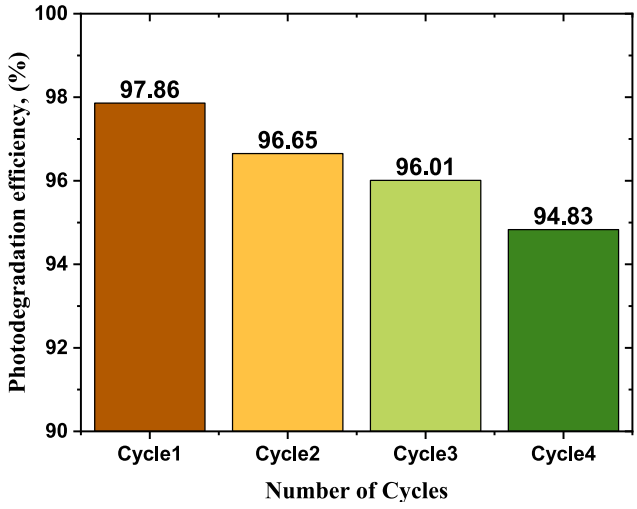

Fig. 12. Photodegradation efficiency and rate per cycle using ZnO:Fe(3 %) catalyst.

sites, improving interactions with pollutants and boosting the degradation rate [44].

An additional key finding is the rise in oxygen defects and the expanded surface area observed in the Fe-doped ZnO samples. These aspects significantly elevate both photocatalytic and antimicrobial activities [45]. The increased surface area, resulting from the morphological transformation from sub-microrods to sub-microsheets due to doping, provides additional sites for interactions with light, pollutants, and microbes, enhancing the material's effectiveness [46,47].

The role of Fe in augmenting the photocatalytic efficiency of ZnO is noteworthy. ZnO alone is a robust photocatalyst, but adding Fe alters its electronic configuration. This alteration is manifested by a noticeable redshift in the absorption spectra, leading to enhanced absorption of visible light. Such enhancement promotes the generation and separation of photogenerated charge carriers, which are pivotal in photocatalytic reactions [48].

XRD analysis has provided insights into the crystal structures of the pure ZnO and its Fe-doped variant. A significant takeaway is the confirmation of the hexagonal wurtzite structure, typical of ZnO, aligning with the findings of several studies [49]. The analysis also

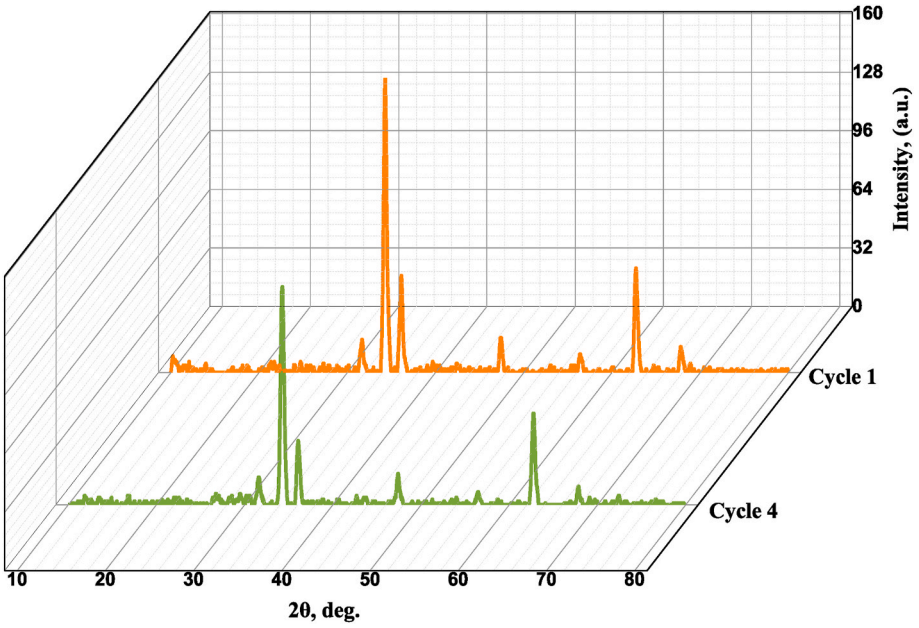

Fig. 13. XRD patterns of ZnO:$Fe_{(3\ \%)}$ catalyst after 1st and fifth cycle stability tests.

Table 4
ZOI of the various microorganisms.

Pathogen	Antibiotic*	A	Pure ZnO	ZnO: $Fe_{(1\ \%)}$	ZnO: $Fe_{(1.5\ \%)}$	ZnO: $Fe_{(3\ \%)}$
Staphylococcus aureus	G	28 ± 0.24	33 ± 0.18	35 ± 0.42	35 ± 0.51	40 ± 0.30
Bacillus subtilis	G	21 ± 0.28	15 ± 0.36	18 ± 0.41	20 ± 0.34	23 ± 0.30
Escherichia coli	G	23 ± 0.33	24 ± 0.26	25 ± 0.05	26 ± 0.52	30 ± 0.31
Klebsiella pneumonia	G	30 ± 0.10	36 ± 0.23	40 ± 0.37	40 ± 0.33	46 ± 0.18
Candida albicans	NY	16 ± 0.42	30 ± 0.21	30 ± 0.42	31 ± 0.32	35 ± 0.43

[a]G = Gentamicin NY = Nystatin. All values are in mm.
[b]ZOI of the positive control. Antimicrobial tests were conducted four times.

Table 5
Comparison of this study's ZOI with multiple others.

Pathogens	Materials	ZOI (mm)	Ref.
Escherichia coli	ZnO:$Fe_{(3\ \%)}$	30 ± 0.31	This study
	Pure ZnO	14 ± 0.3	[20]
	ZnO:$Fe_{(0.025\ mg)}$	18 ± 0.2	[20]
Staphylococcus aureus	**ZnO:$Fe_{(3\ \%)}$**	**40 ± 0.30**	**This study**
	ZnO:$Mg_{(7.5\ \%)}$	19 ± 0.3	[38]
	ZnO:$Ni_{(5\ \%)}$	13 ± 0.14	[39]
Bacillus subtilis	**ZnO:Fe $_{(3\ \%)}$**	**23 ± 0.30**	**This study**
	ZnO:$Al_{(3\ \%)}$	8	[40]
	Pure ZnO	15.5	[41]
Klebsiella pneumonia	**ZnO:Fe $_{(3\ \%)}$**	**46 ± 0.18**	**This study**
	ZnO:$Ag_{(4.5\ \%)}$	45	[29]
Candida albicans	**ZnO:Fe $_{(3\ \%)}$**	**35 ± 0.43**	**This study**
	ZnO:$Ag_{(4.5\ \%)}$	40	[29]
	ZnO:$Ni_{(1\ \%)}$	10 ± 0.12	[39]

highlighted a shift to lower diffraction angles and an increase in FWHM as the level of Fe doping rises, a trend observed in other research [50].

The change from sub-microrods to sub-microsheets upon Fe doping is significant on the morphological front. This transformation, though prominent, is in line with previous findings that emphasize its impact on material properties [51]. The stoichiometry analysis revealed a nearly 1:1 zinc-to-oxygen ratio in the undoped ZnO samples, which is crucial for optimal material performance. Any deviation from this balance can introduce impurities that adversely affect the material's functionality in optoelectronics and semiconductor applications.

The material's direct band gap is consistent with other studies, validating the electronic transitions between the valence and conduction bands [52]. The absorption edge's redshift due to Fe doping highlights its significance in modulating ZnO's optical properties. The FTIR spectroscopy results reiterate Ferin Fathima A. et al.'s findings, showcasing ZnO's consistent vibrational properties across different doping levels and its vulnerability to environmental interactions [53].

Increasing doping concentration significantly influences the characterization of materials as observed through techniques such as SEM, XRD, optical properties assessment, and FTIR. SEM reveals changes in surface morphology like grain size and roughness; XRD shows shifts in peak positions and new peak emergence, indicating alterations in crystal structure; optical property measurements demonstrate shifts in absorption peaks and changes in material transparency, crucial for optoelectronic applications; and FTIR spectra highlight shifts in absorption bands and the appearance of new bands, suggesting changes in chemical bonding. These correlations provide a holistic understanding of how doping impacts the structural, optical, and chemical properties of materials, essential for optimizing their performance in various applications [53].

The influence of increasing doping concentrations of Fe in ZnO on UV–visible absorption spectra and photocatalytic activity in the degradation of paracetamol reveals that higher Fe concentrations lead to shifts in the absorption spectrum, likely due to band gap alterations in ZnO from Fe incorporation, which modifies its electronic structure. This allows the doped ZnO to absorb a broader spectrum of light, enhancing photocatalytic degradation efficiency by improving charge separation and reducing electron-hole pair recombination. Additionally, Fe ions might introduce more catalytic sites or modify ZnO's surface properties, thus increasing interaction with paracetamol molecules. However, while increased doping enhances photocatalytic activity, there appears to be an optimal Fe concentration, beyond which the efficiency might decline due to potential aggregation of Fe particles or creation of excessive trap sites that serve as recombination centers for charge carriers,

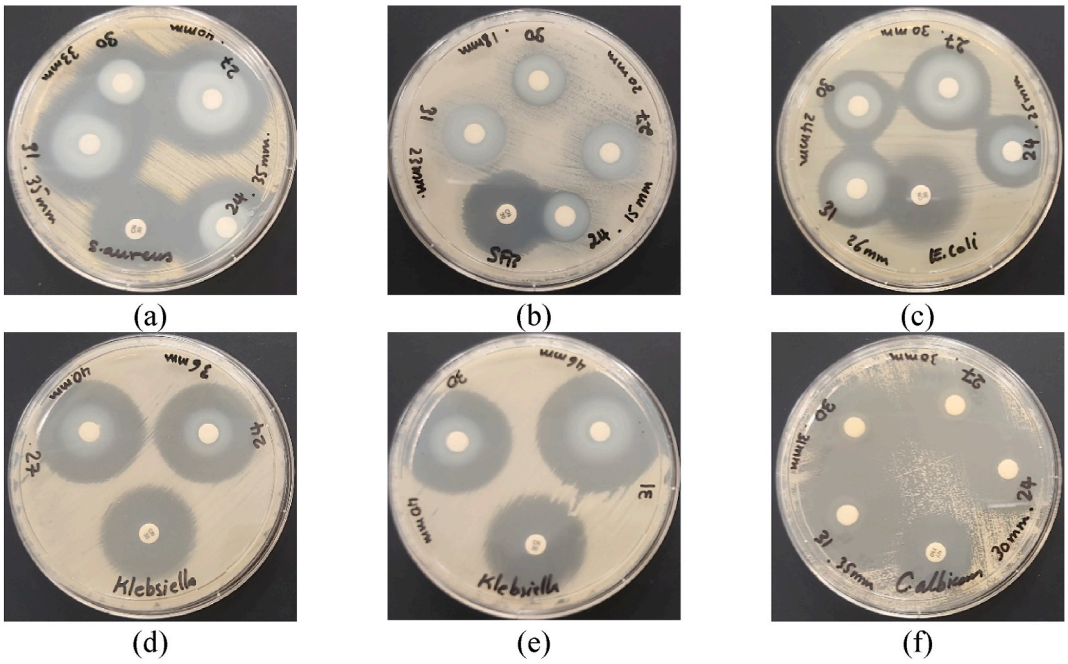

Fig. 14. Schematic of paracetamol degradation mechanism.

highlighting a non-linear relationship between doping concentration and photocatalytic efficiency.

Regarding antimicrobial activity, the synthesized ZnO sub-microparticles displayed selective inhibitory effects on various bacterial strains and fungi. This observation is supported by studies where ZnO sub-microparticles demonstrated size-dependent antimicrobial activity against gram-positive and gram-negative bacteria [54]. The antimicrobial mechanism of ZnO sub-microparticles is linked to their ability to compromise bacterial cell membranes and induce oxidative stress, culminating in cell death [55].

The antimicrobial effectiveness of ZnO is notably enhanced when doped with various metals, such as iron, a finding supported by numerous research studies [41,56]. When metals like silver, copper, or iron are incorporated into ZnO, there is a marked improvement in its ability to fend off microbial activity [53]. The cooperative effect noted in the experiments, especially with the addition of iron to ZnO, aligns with the prevailing theory that doping can alter the surface characteristics of ZnO sub-microparticles, enhancing their proficiency in engaging and disrupting microbial entities [55].

However, it is worth noting that the diminished suppression of *B. subtilis* by pure ZnO diverges from several studies consistently highlighting ZnO's broad-spectrum antimicrobial properties [55]. This variation underscores the intricate nature of the microbial response, which the synthesis methods, particle size, and other physicochemical attributes can influence. Moreover, the differential reaction observed in fungal strains, such as *C. albicans*, aligns with previous findings that fungi generally demand higher ZnO concentrations to be effectively inhibited [57].

Increasing the doping concentration in ZnO-NSs significantly influences their antimicrobial activity, primarily through enhanced reactive oxygen species generation and increased surface area with more active sites. Doping modifies the ZnO-NSs' physical and chemical properties, such as tuning the band-gap to improve light absorption and photocatalytic activity under UV or visible light. This alteration can lead to more effective microbial cell membrane disruption. Moreover, different doping elements and levels can specifically target various microbial species, enhancing the spectrum of antimicrobial action. Higher doping concentrations also affect the material's stability and solubility, which are crucial for the longevity and reusability of ZnO-NSs in antimicrobial applications. Therefore, understanding and optimizing doping levels is vital for tailoring ZnO-NSs' effectiveness against specific pathogens in healthcare and environmental applications.

4.1. Proposed photocatalytic mechanism

Fig. 14 shows photocatalytic mechanisms in undoped and iron-

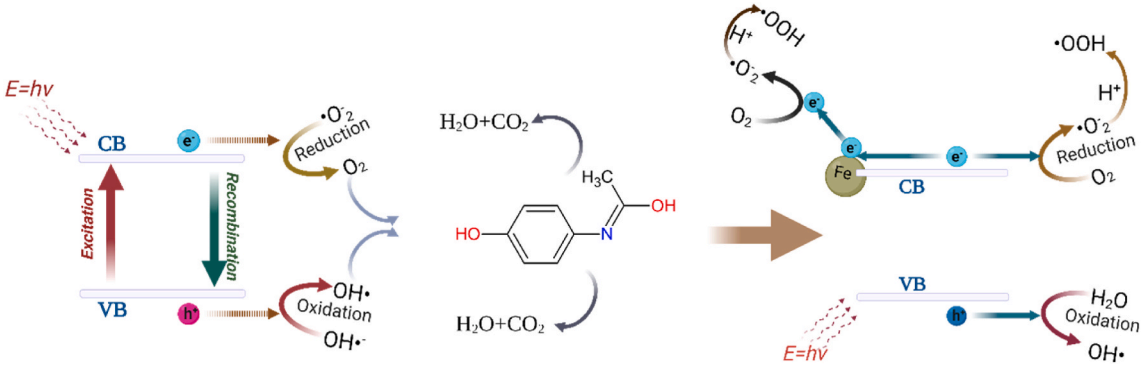

Fig. 15. Antibiotics and ZnO samples (Pure, ZnO:Fe(1–3%)) tested against (a) S. aureus, (b) B. subtilis, (c) E. coli, (d) and (e) K. pneumonia, (f) C. albicans.

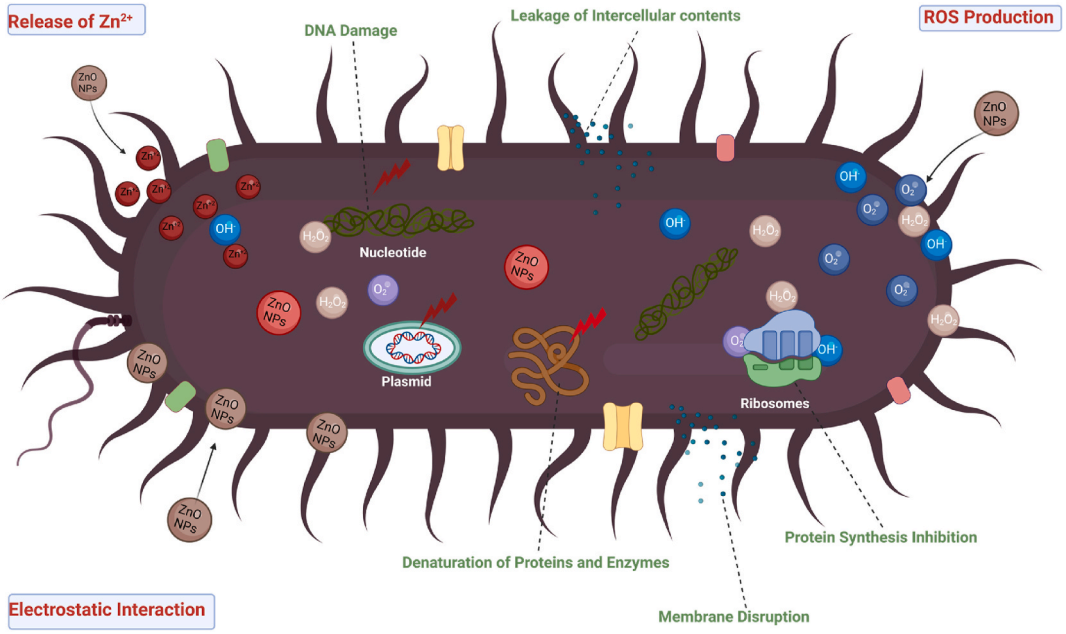

Fig. 16. An illustration of ZnO's antimicrobial mechanisms.

doped ZnO sub-microparticles. Light exposure causes electrons in ZnO to move from the valence to the conduction band, creating electron-hole pairs. These pairs oxidize water molecules and OH- ions at the surface, forming hydroxyl radicals (•OH) and converting atmospheric oxygen into superoxide radicals (•O2-). The recombination of these electron-hole pairs can reduce efficiency, but iron doping mitigates this by trapping charge carriers, prolonging their life, and increasing surface interactions, especially with paracetamol molecules. There are two recombination types: volume and surface, the latter dominating when photoinduced carriers quickly reach the sub-microstructure's surface [58].

Analytical investigations employing XRD and SEM techniques have demonstrated that iron doping diminishes the average size of ZnO sub-microstructure crystallites and modifies their shape, changing them from sub-microrods to sub-microsheets. This alteration in morphology increases the surface area of ZnO, providing more active sites for the adsorption of reactant molecules, thereby enhancing the photocatalytic performance. Furthermore, iron doping brings about two additional advantages: it reduces the band gap of ZnO, increases the availability of charge carriers for the photocatalytic reaction, and raises the level of water adsorbed by ZnO. The increase in water adsorption strengthens water's affinity to the ZnO surface, further improving the photocatalytic efficiency of the catalyst [29,59].

$$ZnO + h\nu \rightarrow ZnO\left(e_{CB}^{-} + h_{VB}^{+}\right), \quad (11)$$

$$H_2O + h_{VB}^{+} \rightarrow OH^{-} + H^{+}, \quad (12)$$

$$e_{CB}^{-} + O_2 \rightarrow \bullet O_2^{-}, \quad (13)$$

$$\bullet O_2^{-} + H^{+} \rightarrow H_2O_2, \quad (14)$$

$$HO_2 + H^{+} + \bullet O_2^{-} \rightarrow H_2O_2 + O_2, \quad (15)$$

$$H_2O_2 + e_{CB}^{-} \rightarrow OH^{-} + \bullet OH, \quad (16)$$

$$h_{VB}^{+} + OH^{-} \rightarrow \cdot OH, \quad (17)$$

$$OH^{-} + \bullet O_2^{-} + Pollutent \rightarrow Degradation\ Products, \quad (18)$$

4.2. Zinc's antimicrobial mechanisms

ZnO exhibits antimicrobial properties by producing ROS like O^{2-}, OH^{-}, and H_2O_2, causing oxidative stress and cellular damage in nucleic acids and lipids, leading to cell death. Additionally, ZnO releases Zn^{2+} ions, disrupting vital cellular functions such as active transport and enzyme activity. Its interaction with bacterial cell membranes, through electrostatic forces, reduces membrane integrity, alters metabolism, and causes leakage of intracellular contents (see Fig. 16). ZnO's broad antimicrobial effectiveness offers a promising alternative to conventional antibiotics, especially considering growing concerns over antibiotic resistance [55–64].

5. Conclusion

Examining ZnO sub-microparticles synthesized via LACBS, both undoped and iron-doped, revealed vital structural and functional insights. X-ray diffraction confirmed ZnO's hexagonal wurtzite crystal structure, while iron doping transformed the morphology from sub-microrods to sub-microsheets, offering various application potentials. Notably, Fe-doped ZnO, particularly at 3 % doping, showed enhanced photocatalytic activity for paracetamol degradation under blue laser light, demonstrating sustained performance over multiple cycles. Additionally, the doped ZnO exhibited improved antimicrobial properties, making it a promising candidate for sustainable photocatalysis and antimicrobial applications.

Funding

This work was kindly supported by the Deanship of Graduate Studies and Research, Ajman University, Ajman, United Arab Emirates, for the financial assistance through Grant number (Project ID, DGSR Ref. Number: 2023-IRG-HBS-11).

Institutional review board statement

Not applicable.

Informed consent statement

Not applicable.

CRediT authorship contribution statement

Samer H. Zyoud: Writing – review & editing, Writing – original draft, Visualization, Validation, Supervision, Software, Resources, Project administration, Methodology, Investigation, Funding acquisition, Formal analysis, Data curation, Conceptualization. **Che Azurahanim Che Abdullah:** Writing – review & editing, Writing – original draft. **Akram Ashames:** Resources, Data curation. **Nageeb Hassan:** Resources, Data curation. **Ibrahim S. Yahia:** Writing – original draft, Methodology. **Ahed H. Zyoud:** Visualization, Validation, Methodology, Conceptualization. **Heba Y. Zahran:** Software. **Naser Qamhieh:** Resources, Data curation. **Ghaseb N. Makhadmeh:** Software, Investigation. **Tariq AlZoubi:** Formal analysis.

Declaration of competing interest

The authors declare that they have no known competing financial interests or personal relationships that could have appeared to influence the work reported in this paper.

Data availability

All data are contained within the article.

References

[1] R.A. Rayan, Pharmaceutical effluent evokes superbugs in the environment: a call to action, Biosaf. Health (2023), https://doi.org/10.1016/j.bsheal.2023.10.005.

[2] M.D.C. Gómez-Regalado, J. Martín, J.L. Santos, I. Aparicio, E. Alonso, A. Zafra-Gómez, Bioaccumulation/bioconcentration of pharmaceutical active compounds in aquatic organisms: assessment and factors database, Sci. Total Environ. 861 (2023) 160638, https://doi.org/10.1016/j.scitotenv.2022.160638.

[3] D. Muir, D. Simmons, X. Wang, T. Peart, M. Villella, J. Miller, J. Sherry, Bioaccumulation of pharmaceuticals and personal care product chemicals in fish exposed to wastewater effluent in an urban wetland, Sci. Rep. 7 (2017) 16999, https://doi.org/10.1038/s41598-017-15462-x.

[4] M. Zupanc, T. Kosjek, M. Petkovšek, M. Dular, B. Kompare, B. Širok, Ž. Blažeka, E. Heath, Removal of pharmaceuticals from wastewater by biological processes, hydrodynamic cavitation and UV treatment, Ultrason. Sonochem. 20 (2013) 1104–1112, https://doi.org/10.1016/j.ultsonch.2012.12.003.

[5] Z. Xie, G. Lu, Z. Yan, J. Liu, P. Wang, Y. Wang, Bioaccumulation and trophic transfer of pharmaceuticals in food webs from a large freshwater lake, Environ. Pollut. 222 (2017) 356–366, https://doi.org/10.1016/j.envpol.2016.12.026.

[6] I.M.D. Gonzaga, C.V.S. Almeida, L.H. Mascaro, A critical review of photo-based advanced oxidation processes to pharmaceutical degradation, Catalysts 13 (2023) 221, https://doi.org/10.3390/catal13020221.

[7] Y. Wang, W. Duan, B. Liu, X. Chen, F. Yang, J. Guo, The effects of doping copper and mesoporous structure on photocatalytic properties of TiO_2, J. Nanomater. 2014 (2014) e178152, https://doi.org/10.1155/2014/178152.

[8] S.H. Zyoud, I.S. Yahia, M. Shahwan, A.H. Zyoud, H.Y. Zahran, M.S. Abdel-wahab, M.G. Daher, M. Nasor, G.N. Makhadmeh, N. Hassan, A. Ashames, N. Qamhieh, Fast and excellent enhanced photocatalytic degradation of methylene blue using silver-doped zinc oxide submicron structures under blue laser irradiation, Cryst 13 (2023) 229, https://doi.org/10.3390/CRYST13020229. Page 229 13 (2023).

[9] J. Gonz醴ez-Fern醬dez, D.D. Pinz髇-Moreno, A.A. Neciosup-Puican, M. V. Carranza-Oropeza, Green method, optical and structural characterization of ZnO nanoparticles synthesized using leaves extract of *M. oleifera*, J. Renew. Mater. 10 (2021) 833–847, https://doi.org/10.32604/JRM.2021.017377.

[10] K. Singh, Neha, M. Kumar, H. Singh, G. Singh, ZnO NPs: photocatalytic potential, mechanistic insights, favorable parameters and challenges, Mater. Today Proc. (2023), https://doi.org/10.1016/j.matpr.2023.03.002.

[11] K. Qi, B. Cheng, J. Yu, W. Ho, Review on the improvement of the photocatalytic and antibacterial activities of ZnO, J. Alloys Compd. 727 (2017) 792–820, https://doi.org/10.1016/j.jallcom.2017.08.142.

[12] A.E. Ramírez, M. Montero-Muñoz, L.L. López, J.E. Ramos-Ibarra, J.A.H. Coaquira, B. Heinrichs, C.A. Páez, Significantly enhancement of sunlight photocatalytic performance of ZnO by doping with transition metal oxides, Sci. Rep. 11 (2021) 2804, https://doi.org/10.1038/s41598-020-78568-9.

[13] H. Salehzadeh, K. Wantala, E. Mohammadi, H.P. Shivaraju, B. Shahmoradi, S. Rtimi, A. Maleki, M. Safari, Solar photodegradation of malathion from aqueous media using Al-doped ZnO/Fe3O4 nanocomposite, Catal. Commun. 184 (2023) 106785, https://doi.org/10.1016/j.catcom.2023.106785.

[14] Y.S. Seo, S.-G. Oh, Controlling the recombination of electron-hole pairs by changing the shape of ZnO nanorods via sol-gel method using water and their enhanced photocatalytic properties, Korean J. Chem. Eng. 36 (2019) 2118–2124, https://doi.org/10.1007/s11814-019-0401-0.

[15] T. Mao, M. Liu, L. Lin, Y. Cheng, C. Fang, A study on doping and compound of zinc oxide photocatalysts, Polymers 14 (2022) 4484, https://doi.org/10.3390/polym14214484.

[16] E.T.D. Kumar, S. Easwaramoorthi, R.R. J, Cd2V2O7–ZnO mixed oxide for extended wavelength absorption with suppressed charge carrier recombination: a photocatalytic material, Mater. Chem. Phys. 289 (2022) 126484, https://doi.org/10.1016/j.matchemphys.2022.126484.

[17] Y.G. Habba, M. Capochichi-Gnambodoe, Y. Leprince-Wang, Enhanced photocatalytic activity of iron-doped ZnO nanowires for water purification, Appl. Sci. 7 (2017) 1185, https://doi.org/10.3390/app7111185.

[18] R. Liu, Y. Zhang, L. Duan, X. Zhao, Effect of Fe2+/Fe3+ ratio on photocatalytic activities of Zn1-Fe O nanoparticles fabricated by the auto combustion method, Ceram. Int. 46 (2019), https://doi.org/10.1016/j.ceramint.2019.08.074.

[19] S. Thakur, S. Neogi, Effect of doped ZnO nanoparticles on bacterial cell morphology and biochemical composition, Appl. Nanosci. 11 (2020), https://doi.org/10.1007/s13204-020-01592-8.

[20] S. Aiswarya Devi, M. Harshiny, S. Udaykumar, P. Gopinath, M. Matheswaran, Strategy of metal iron doping and green-mediated ZnO nanoparticles: dissolubility, antibacterial and cytotoxic traits †Electronic supplementary information (ESI) available, Toxicol. Res. 6 (2017) 854–865, https://doi.org/10.1039/c7tx00093f. See DOI: 10.1039/c7tx00093f.

[21] R. Kumar, M. Nayak, G.C. Sahoo, K. Pandey, M.C. Sarkar, Y. Ansari, V.N.R. Das, R. K. Topno, null Bhawna, M. Madhukar, P. Das, Iron oxide nanoparticles based antiviral activity of H1N1 influenza A virus, J. Infect. Chemother. Off. J. Jpn. Soc. Chemother. 25 (2019) 325–329, https://doi.org/10.1016/j.jiac.2018.12.006.

[22] S.H. Zyoud, O.E. Hegazi, S.O. Alalalmeh, C. Azurahanim Che Abdullah, A. Ashames, Nageeb Hassan, I.S. Yahia, A.H. Zyoud, M.G. Daher, M. Shahwan, S. Haj Bloukh, H.Y. Zahran, N. Qamhieh, M. Nasor, A. Jairoun, Enhancing antimicrobial and photocatalyst properties of Mg-doped ZnO nanotubes via a novel laser-assisted chemical bath synthesis, J. Saudi Chem. Soc. (2023) 101752, https://doi.org/10.1016/j.jscs.2023.101752.

[23] S.H. Zyoud, N.M. Ahmed, A.S.Z. Lahewil, A.F. Omar, Micro spot ZnO nanotubes using laser assisted chemical bath deposition: a low-cost approach to UV photodetector fabrication, Sens. Actuators Phys. 338 (2022) 113485, https://doi.org/10.1016/J.SNA.2022.113485.

[24] X. Li, H. Zheng, Y. Wang, X. Li, J. Liu, K. Yan, J. Wang, K. Zhu, Synergistic effect of Y doping and reduction of TiO2 on the improvement of photocatalytic performance, Nanomaterials 13 (2023) 2266, https://doi.org/10.3390/nano13152266.

[25] S.S. Mohtar, F. Aziz, A.F. Ismail, N.S. Sambudi, H. Abdullah, A.N. Rosli, B. Ohtani, Impact of doping and additive applications on photocatalyst textural properties in removing organic pollutants: a review, Catalysts 11 (2021) 1160, https://doi.org/10.3390/catal11101160.

[26] S.H. Zyoud, S.O. Alalalmeh, O.E. Hegazi, I.S. Yahia, H.Y. Zahran, H.A. Sara, S. H. Bloukh, M. Shahwan, A.H. Zyoud, N. Hassan, A. Ashames, M.G. Daher, G. N. Makhadmeh, A. Jairoun, N. Qamhieh, M.S. Abdel-wahab, Novel laser-assisted chemical bath synthesis of pure and silver-doped zinc oxide nanoparticles with improved antimicrobial and photocatalytic properties, Catalysts 13 (2023) 900, https://doi.org/10.3390/catal13050900.

[27] S.H. Zyoud, O.E. Hegazi, S.O. Alalalmeh, I.S. Yahia, H.Y. Zahran, S.H. Bloukh, H. A. Sara, A.H. Zyoud, M. Shahwan, A. Ashames, N. Hassan, M.G. Daher, G. N. Makhadmeh, A.A. Jairoun, E.A. Kamoun, Enhanced photocatalytic and antimicrobial properties of undoped and aluminum-doped zinc oxide nanosheets synthesized via novel laser-assisted chemical bath technique, Appl. Phys. A 129 (2023) 750, https://doi.org/10.1007/s00339-023-07033-x.

[28] A.S.Z. Lahewil, S.H. Zyoud, N.M. Ahmed, A.F. Omar, N.Z.N. Azman, Synthesis ZnO nanoclusters micro active area using continues wave blue laser-assisted chemical bath deposition based on UV photodetector, Optik 260 (2022) 169099, https://doi.org/10.1016/j.ijleo.2022.169099.

[29] S.H. Zyoud, S.O. Alalalmeh, O.E. Hegazi, I.S. Yahia, H.Y. Zahran, H.A. Sara, S. H. Bloukh, M. Shahwan, A.H. Zyoud, N. Hassan, A. Ashames, M.G. Daher, G. N. Makhadmeh, A. Jairoun, N. Qamhieh, M.S. Abdel-wahab, Novel laser-assisted chemical bath synthesis of pure and silver-doped zinc oxide nanoparticles with improved antimicrobial and photocatalytic properties, Catal 13 (2023) 900, https://doi.org/10.3390/CATAL13050900. Page 900 13 (2023).

[30] L. Qin, F.J. Mawignon, M. Hussain, N.K. Ange, S. Lu, M. Hafezi, G. Dong, Economic friendly ZnO-based UV sensors using hydrothermal growth: a review, Mater 14 (2021) 4083, https://doi.org/10.3390/MA14154083. Page 4083 14 (2021).

[31] E. Wagner, W. Maudez, S. Bagdzevicius, S.C. Sandu, G. Benvenuti, Chemical beam vapour deposition technique with Sybilla equipment: review of main results in its 20-year anniversary, 64, https://doi.org/10.1117/12.2591443, 2021.

[32] O. Pakma, C. Özaydın, Ş. Özden, I.A. Kariper, Ö. Güllü, Synthesis and characterization of vanadium oxide thin films on different substrates, J. Mater. Sci. Mater. Electron. 28 (2017) 10909–10913, https://doi.org/10.1007/S10854-017-6870-1/METRICS.

[33] A. Vasala, V.P. Hytönen, O.H. Laitinen, Modern tools for rapid diagnostics of antimicrobial resistance, Front. Cell. Infect. Microbiol. 10 (2020) 308, https://doi.org/10.3389/FCIMB.2020.00308.

[34] V.H.-T. Thi, B.-K. Lee, Effective photocatalytic degradation of paracetamol using La-doped ZnO photocatalyst under visible light irradiation, Mater. Res. Bull. 96 (2017) 171–182, https://doi.org/10.1016/j.materresbull.2017.04.028.

[35] E.S. Elmolla, M. Chaudhuri, Comparison of different advanced oxidation processes for treatment of antibiotic aqueous solution, Desalination 256 (2010) 43–47, https://doi.org/10.1016/j.desal.2010.02.019.
[36] R. Al Abri, F. Al Marzouqi, A.T. Kuvarega, M.A. Meetani, S.M.Z. Al Kindy, S. Karthikeyan, Y. Kim, R. Selvaraj, Nanostructured cerium-doped ZnO for photocatalytic degradation of pharmaceuticals in aqueous solution, J. Photochem. Photobiol. Chem. 384 (2019) 112065, https://doi.org/10.1016/j.jphotochem.2019.112065.
[37] M. Farzadkia, A. Esrafili, M.Ali Baghapour, Y.D. Shahamat, N. Okhovat, Degradation of metronidazole in aqueous solution by nano-ZnO/UV photocatalytic process, Desalination Water Treat. 52 (2014) 4947–4952, https://doi.org/10.1080/19443994.2013.810322.
[38] K.P. raj, K. Sadaiyandi, A. Kennedy, S. Sagadevan, Z.Z. Chowdhury, M.R.B. Johan, F.A. Aziz, R.F. Rafique, R.T. Selvi, R.R. bala, Influence of Mg doping on ZnO nanoparticles for enhanced photocatalytic evaluation and antibacterial analysis, Nanoscale Res. Lett. 13 (2018), https://doi.org/10.1186/S11671-018-2643-X.
[39] G. Faye, T. Jebessa, T. Wubalem, Biosynthesis, characterisation and antimicrobial activity of zinc oxide and nickel doped zinc oxide nanoparticles using Euphorbia abyssinica bark extract, IET Nanobiotechnol. 16 (2022) 25–32, https://doi.org/10.1049/NBT2.12072.
[40] C. Manoharan, G. Pavithra, M. Bououdina, S. Dhanapandian, P. Dhamodharan, Characterization and study of antibacterial activity of spray pyrolysed ZnO:Al thin films, Appl. Nanosci. 6 (2016) 815–825, https://doi.org/10.1007/s13204-015-0493-8.
[41] N. Sharma, J. Kumar, S. Thakur, S. Sharma, V. Shrivastava, Antibacterial study of silver doped zinc oxide nanoparticles against Staphylococcus aureus and Bacillus subtilis, Drug Invent, Today Off. 5 (2013) 50–54, https://doi.org/10.1016/J.DIT.2013.03.007.
[42] N.R. Khalid, A. Hammad, M.B. Tahir, M. Rafique, T. Iqbal, G. Nabi, M.K. Hussain, Enhanced photocatalytic activity of Al and Fe co-doped ZnO nanorods for methylene blue degradation, Ceram. Int. 45 (2019) 21430–21435, https://doi.org/10.1016/j.ceramint.2019.07.132.
[43] P.P. Fu, Q. Xia, H.-M. Hwang, P.C. Ray, H. Yu, Mechanisms of nanotoxicity: generation of reactive oxygen species, J. Food Drug Anal. 22 (2014) 64–75, https://doi.org/10.1016/j.jfda.2014.01.005.
[44] Y. Peng, P. Kan, Q. Zhang, Y. Zhou, Oxygen vacancy enhanced photoreduction Cr (VI) on few-layers BiOBr nanosheets, Catalysts 9 (2019) 558, https://doi.org/10.3390/catal9060558.
[45] S.A. Ayon, M. Jamal, MdM. Billah, S. Neaz, Augmentation of magnetic properties and antimicrobial activities of band gap modified Ho3+ and Sm3+ doped ZnO nanoparticles: a comparative experimental study, J. Alloys Compd. 897 (2022) 163179, https://doi.org/10.1016/j.jallcom.2021.163179.
[46] A. Banerjee, J. Qi, R. Gogoi, J. Wong, S. Mitragotri, Role of nanoparticle size, shape and surface chemistry in oral drug delivery, J. Control. Release Off. J. Control. Release Soc. 238 (2016) 176–185, https://doi.org/10.1016/j.jconrel.2016.07.051.
[47] P. Djinović, J. Batista, J. Levec, A. Pintar, Synthesis of ordered nanostructured CuO-CeO2 catalysts by hard template method, in: E.M. Gaigneaux, M. Devillers, S. Hermans, P.A. Jacobs, J.A. Martens, P. Ruiz (Eds.), Stud. Surf. Sci. Catal., Elsevier, 2010, pp. 245–248, https://doi.org/10.1016/S0167-2991(10)75034-5.
[48] Y.I. Abdulkarim, L. Deng, F.F. Muhammad, L. He, Enhanced light absorption in the organic thin films by coating cross-shaped metamaterial resonators onto the active layers, Results Phys. 13 (2019) 102338, https://doi.org/10.1016/j.rinp.2019.102338.
[49] V. Mohammad, A. Umar, Y.-B. Hahn, ZnO nanoparticles: growth, properties, and applications, in: Met. Oxide Nanostructures Their, Appl., 2010, pp. 1–36.
[50] F.E.S.M Salaken, J. Podder, Effect of Fe-doping on the structural and optical properties of ZnO thin films prepared by spray pyrolysis, J. Semicond. 34 (2013) 073003, https://doi.org/10.1088/1674-4926/34/7/073003.
[51] F. Ahmed, S. Kumar, N. Arshi, M.S. Anwar, B.H. Koo, Morphological evolution between nanorods to nanosheets and room temperature ferromagnetism of Fe-doped ZnO nanostructures, CrystEngComm 14 (2012) 4016–4026, https://doi.org/10.1039/C2CE25227A.
[52] M.A. Hadi, MdN. Islam, J. Podder, Indirect to direct band gap transition through order to disorder transformation of Cs2AgBiBr6via creating antisite defects for optoelectronic and photovoltaic applications, RSC Adv. 12 (2022) 15461–15469, https://doi.org/10.1039/d1ra06308a.
[53] A. Ferin Fathima, R. Jothi Mani, K. Sakthipandi, K. Manimala, A. Hossain, Enhanced antifungal activity of pure and iron-doped ZnO nanoparticles prepared in the absence of reducing agents, J. Inorg. Organomet. Polym. Mater. 30 (2020) 2397–2405, https://doi.org/10.1007/s10904-019-01400-z.
[54] B.L. da Silva, M.P. Abuçafy, E.B. Manaia, J.A.O. Junior, B.G. Chiari-Andréo, R.C.L. R. Pietro, L.A. Chiavacci, Relationship between structure and antimicrobial activity of zinc oxide nanoparticles: an overview, Int. J. Nanomedicine 14 (2019) 9395, https://doi.org/10.2147/IJN.S216204.
[55] A. Sirelkhatim, S. Mahmud, A. Seeni, N.H.M. Kaus, L.C. Ann, S.K.M. Bakhori, H. Hasan, D. Mohamad, Review on zinc oxide nanoparticles: antibacterial activity and toxicity mechanism, Nano-Micro Lett. 7 (2015) 219–242, https://doi.org/10.1007/S40820-015-0040-X.
[56] I.A. Hassan, S. Sathasivam, S.P. Nair, C.J. Carmalt, Antimicrobial properties of copper-doped ZnO coatings under darkness and white light illumination, ACS Omega 2 (2017) 4556–4562, https://doi.org/10.1021/acsomega.7b00759.
[57] S. Gunalan, R. Sivaraj, V. Rajendran, Green synthesized ZnO nanoparticles against bacterial and fungal pathogens, Prog. Nat. Sci. Mater. Int. 22 (2012) 693–700, https://doi.org/10.1016/j.pnsc.2012.11.015.
[58] S. Liu, G. Huang, J. Wang, J. Bao, M. Wang, Y. Wei, Y. Zhong, F. Bai, Noble metal nanoparticle-loaded porphyrin hexagonal submicrowires composites (M-HW): photocatalytic synthesis and enhanced photocatalytic activity, Nanomater 13 (2023) 660, https://doi.org/10.3390/NANO13040660. Page 660 13 (2023).
[59] S. Ghosh, V.S. Goudar, K.G. Padmalekha, S.V. Bhat, S.S. Indi, H.N. Vasan, ZnO/Ag nanohybrid: synthesis, characterization, synergistic antibacterial activity and its mechanism, RSC Adv. 2 (2012) 930–940, https://doi.org/10.1039/C1RA00815C.
[60] M.T. Yassin, A.A.F. Mostafa, A.A. Al-Askar, F.O. Al-Otibi, Facile green synthesis of zinc oxide nanoparticles with potential synergistic activity with common antifungal agents against multidrug-resistant candidal strains, Cryst 12 (2022) 774, https://doi.org/10.3390/CRYST12060774. Page 774 12 (2022).
[61] A. Maleki, B. Shahmoradi, Solar degradation of Direct Blue 71 using surface modified iron doped ZnO hybrid nanomaterials, Water Sci. Technol. 65 (11) (2012 Jun 1) 1923–1928.
[62] A. Maleki, F. Moradi, B. Shahmoradi, R. Rezaee, S.M. Lee, The photocatalytic removal of diazinon from aqueous solutions using tungsten oxide doped zinc oxide nanoparticles immobilized on glass substrate, J. Mol. Liq. 297 (2020 Jan 1) 111918.
[63] H. Salehzadeh, K. Wantala, E. Mohammadi, H.P. Shivaraju, B. Shahmoradi, S. Rtimi, A. Maleki, M. Safari, Solar photodegradation of malathion from aqueous media using Al-doped ZnO/Fe3O4 nanocomposite, Catal. Commun. 184 (2023 Nov 1) 106785.
[64] S. Kohzadi, A. Maleki, M. Bundschuh, Z. Vahabzadeh, S.A. Johari, R. Rezaee, B. Shahmoradi, N. Marzban, N. Amini, Doping zinc oxide (ZnO) nanoparticles with molybdenum boosts photocatalytic degradation of Rhodamine b (RhB): particle characterization, degradation kinetics and aquatic toxicity testing, J. Mol. Liq. 385 (2023 Sep 1) 122412.